

Creating multicomponent Schrödinger cat states in a coupled qubit-oscillator system

Pavel Stránský^{1,*} and Pavel Cejnar^{1,†}

¹*Institute of Particle and Nuclear Physics, Faculty of Mathematics and Physics, Charles University, V Holešovičkách 2, 18000 Prague, Czechia*

(Dated: December 30, 2025)

We present a method for preparing various exotic modifications of Schrödinger cat states by coupling a semiclassical oscillator to a system of qubits. Varying the number of qubits and parameters of the quantum quench performed in the coupled system, we bring the oscillator into a highly non-classical state composed of an arbitrary number of partly coherent wavepackets in tunable proportions and motion relations. The method can be implemented with the aid of current experimental techniques and may find applications in quantum information and sensing protocols.

While in the early years of quantum theory the celebrated puzzle of Schrödinger's cat [1], which was thought in the $|\text{dead}\rangle + |\text{alive}\rangle$ quantum superposition state, served to metaphorically demonstrate the inherent strangeness of quantum laws, at present the so-called Schrödinger-cat states [2–13] play the role of an essential quantum resource. Such states, whose laboratory realizations were reported on the platforms ranging from quantum optics to superconducting circuits and trapped ions, can be applied in quantum information and communication as robust realizations of qubits [14–20], but also in quantum metrology due to the sub-Planck phase-space structures they typically exhibit [21–23].

The original motivation for studying the cat-like states was to explore possibilities of creating *almost pure* superposition states in large (nearly macroscopic) quantum systems (see, e.g., Ref. [10]). However, also the cat-like superpositions that show *maximal entanglement* of a large system with some ancillary qubits (so-called Bell cat states, in which the large system alone is in a fully incoherent mixed state) are of great importance from both fundamental and application points of view [24, 25]. In this Letter, we present an implementable method for creating exotic cat-like states, which are somewhere in between the above two extremal cases. Bringing the semiclassical system, namely an oscillator, into a *partially entangled* superposition state with a set of qubits, we generate highly non-classical behavior characterized by $n \geq 2$ macroscopically distinguishable and partly coherent wavepackets moving in the oscillator phase space (cf. Refs. [26–29]). Parameters of these wavepackets (their mutual proportions and dynamical relations) can be engineered with respect to potential applications. These curious states and the way of their preparation represent an instructive and amusing demonstration of complex behavior generated in one of the simplest quantum systems.

We use a generalized Rabi model, which describes the spin of length $j = N/2$ with $N = 1, 2, 3, \dots$ coupled to a quantum oscillator [30–32] (see also [33, 34]). The spin—its $(2j+1)$ -dimensional Hilbert space—can be realized via an ensemble of N qubits restricted to the

subspace of fully exchange-symmetric states. This system can be experimentally implemented with the aid of trapped ions, macroscopic mechanical oscillators or superconducting circuits, see, e.g., Refs. [35–44]. Denoting by \hat{b}^\dagger and \hat{b} the creation and annihilation operators of the bosonic oscillator quanta and by $\hat{J}_\pm = \hat{J}_x \pm i\hat{J}_y$, $\hat{J}_0 = \hat{J}_z$ the angular-momentum operators of the spin (for qubits $\hat{\mathbf{J}} = \frac{1}{2} \sum_{i=1}^N \hat{\boldsymbol{\sigma}}_i$, where $\hat{\boldsymbol{\sigma}}_i$ is the vector of Pauli matrices acting in the i th-qubit space), the Hamiltonian reads as

$$\frac{\hat{H}(\lambda)}{\omega} = \hat{b}^\dagger \hat{b} + R(\hat{J}_0 + j) + \lambda \sqrt{\frac{R}{8j}} [(1+\delta)(\hat{b}^\dagger \hat{J}_- + \hat{b} \hat{J}_+) + (1-\delta)(\hat{b}^\dagger \hat{J}_+ + \hat{b} \hat{J}_-)], \quad (1)$$

where ω and $R\omega$, respectively, are energies of the elementary oscillator and spin excitations, and λ is a dimensionless spin-oscillator coupling strength. The character of the spin-oscillator interaction is varied by parameter δ between the Janes-Cummings ($\delta = +1$), Dicke ($\delta = 0$) and anti-Janes-Cummings ($\delta = -1$) regimes [31, 32]. Note that the dependence of \hat{H} on δ and R is implicit as these parameters stay fixed in the protocol described below. In the following, we set $\hbar = 1$ and express the energy E and time t in units $\epsilon = 2jR\omega$ and $\tau = 1/\epsilon$, respectively.

We assume that the ratio R between energies of the spin and oscillator elementary excitations satisfies the condition $R \gg 1$, which leads to semiclassical behavior of the oscillator as the average numbers of phonons in most of the system states are very large. This effective size parameter [45] also enters the interaction term to ensure its proportional scaling with respect to the free Hamiltonian [33]. In the limit $R \rightarrow \infty$, the system develops critical points at $\lambda = \pm 1$, where the ground state transforms nonanalytically between the normal ($|\lambda| < 1$) and superradiant ($|\lambda| > 1$) phases, which is connected with spontaneous breaking of the conserved parity $\hat{\Pi} = (-1)^{\hat{b}^\dagger \hat{b} + \hat{J}_0 + j}$. This ground-state quantum phase transition leads to the occurrence of nearly degenerate parity doublets in the low-energy spectrum for $|\lambda| > 1$ and is accompanied by a pattern of excited-state singularities [33, 45].

Our method of creating multicomponent Schrödinger-cat states relies on the quantum quench protocol, in

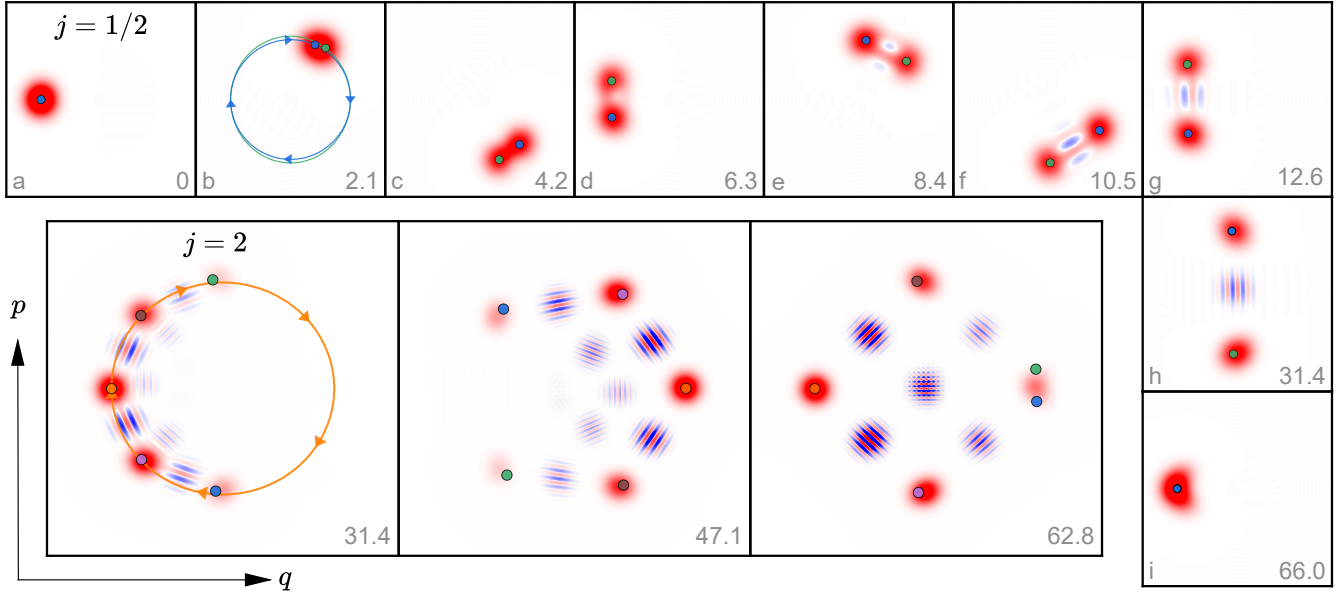


FIG. 1. The evolving oscillator Wigner functions $W_{\text{osc}}(q, p, t)$ (with red/blue indicating positive/negative values) for systems with spins $j = \frac{1}{2}$ and 2 after the quantum quench from $\lambda_{\text{in}} = 1.5$ to $\lambda_{\text{fi}} = -0.283$, with $\delta = 0.5$ and $R = 20$. The evolution starts at $t = 0$ from a single wavepacket in the leftmost ($q < 0$) position. Times t/τ of all snapshots are indicated within the panels (for $j = \frac{1}{2}$ they are also marked in Fig. 3). Color bullets and the oval curves indicate classical trajectories $(q(t), p(t))$. The displayed phase-space domain in all cases is $q, p \in [-1.5, +1.5]$. See videos [48] for full dynamics.

which the spin-oscillator system is prepared nearly in the ground state $|\Psi_{\text{in}}\rangle \approx |\Psi_0(\lambda_{\text{in}})\rangle$ of Hamiltonian $\hat{H}_{\text{in}} \equiv \hat{H}(\lambda_{\text{in}})$ (more precisely, $|\Psi_{\text{in}}\rangle$ coincides with a particular superposition of the lowest energy parity doublet in the superradiant phase) and then the coupling strength is suddenly switched to another value λ_{fi} , yielding Hamiltonian $\hat{H}_{\text{fi}} \equiv \hat{H}(\lambda_{\text{fi}})$. What happens is illustrated in Fig. 1. It shows two examples of the Wigner function $W_{\text{osc}}(q, p, t)$ [46, 47] associated with the density operator $\hat{\rho}_{\text{osc}}(t) = \text{tr}_{\text{sp}}|\Psi(t)\rangle\langle\Psi(t)|$ of the oscillator subsystem evolving after the quench with given parameters. Here $|\Psi(t)\rangle = e^{-i\hat{H}_{\text{fi}}t}|\Psi_{\text{in}}\rangle$ and tr_{sp} is the partial trace over the spin Hilbert space. The figure shows only a few snapshots of the after-quench dynamics. A much clearer picture can be obtained from the attached video files [48].

In general, for the system with a given j we observe $n = 2j + 1 = N + 1$ wavepackets moving in the coordinate $(q) \times$ momentum (p) phase space of the oscillator. The trajectory curves of individual wavepackets are very close, though not identical, but the speeds differ substantially. From time to time various pairs of wavepackets cross each other within short intervals of overlap. We stress that individual wavepackets represent nearly classical states of the oscillator, but their observed combination is a highly nonclassical and coherent quantum state. The semiclassicality is indicated by the agreement of wavepacket trajectories with the classical predictions (which, as noted above, follows from the large value of R), while the quantum coherence is manifested by the ripples

of positive and negative values of $W_{\text{osc}}(q, p, t)$ between each pair of wavepackets.

The explanation of this behavior follows from the conversion of Hamiltonian (1) into the form

$$\frac{\hat{H}(\lambda)}{\omega} = Rj + \hat{b}^\dagger \hat{b} + \hat{\mathbf{B}}(\lambda) \cdot \hat{\mathbf{J}} = \hat{b}^\dagger \hat{b} + |\hat{\mathbf{B}}(\lambda)| \hat{\mathbf{n}}(\lambda) \cdot \hat{\mathbf{J}}, \quad (2)$$

where the vector operator $\hat{\mathbf{J}} \equiv (\hat{J}_x, \hat{J}_y, \hat{J}_z)$ acts in the spin subspace of the full Hilbert space, while vector operators $\hat{\mathbf{B}}$ and $\hat{\mathbf{n}} = \hat{\mathbf{B}}/|\hat{\mathbf{B}}|$ are expressed through \hat{b}^\dagger and \hat{b} defined in the oscillator subspace [49]. Introducing coordinate and momentum operators $\hat{q} = (\hat{b}^\dagger + \hat{b})/\sqrt{4jR}$ and $\hat{p} = i(\hat{b}^\dagger - \hat{b})/\sqrt{4jR}$, we get $\hat{\mathbf{B}} = R(\sqrt{2}\lambda\hat{q}, -\sqrt{2}\lambda\delta\hat{p}, 1)$ and $|\hat{\mathbf{B}}| = R\sqrt{2\lambda^2(\hat{q}^2 + \delta^2\hat{p}^2) + 1}$. When approaching the limit $R \rightarrow \infty$, the commutator $[\hat{q}, \hat{p}] = i/2jR$ vanishes and the observable $\hat{\mathbf{n}} \cdot \hat{\mathbf{J}}$ becomes an approximate integral of motions. For semiclassical (narrow) wavepackets both \hat{q} and \hat{p} can be replaced by their averages \bar{q} and \bar{p} , so the operators $\hat{\mathbf{B}}(\lambda)$ and $\hat{\mathbf{n}}(\lambda)$ become ordinary functions $\mathbf{B}(\bar{q}, \bar{p}, \lambda)$ and $\mathbf{n}(\bar{q}, \bar{p}, \lambda)$ and $\hat{\mathbf{n}} \cdot \hat{\mathbf{J}}$ turns into $\hat{\mathbf{J}} \cdot \mathbf{n}$, which is the spin projection in the direction of the unit vector \mathbf{n} . This leads to full correlation of the spin and oscillator dynamics, when the spin state evolves in a way determined by the motion of the oscillator wavepacket in $q \times p$. In particular, for a given value $m = -j, \dots, +j$ of $\hat{\mathbf{J}} \cdot \mathbf{n}$ the oscillator evolves by an effective Hamiltonian

$$\frac{\hat{H}_{\text{osc}}^{(m)}(\lambda)}{\omega} = \hat{b}^\dagger \hat{b} + |\hat{\mathbf{B}}(\lambda)| m, \quad (3)$$

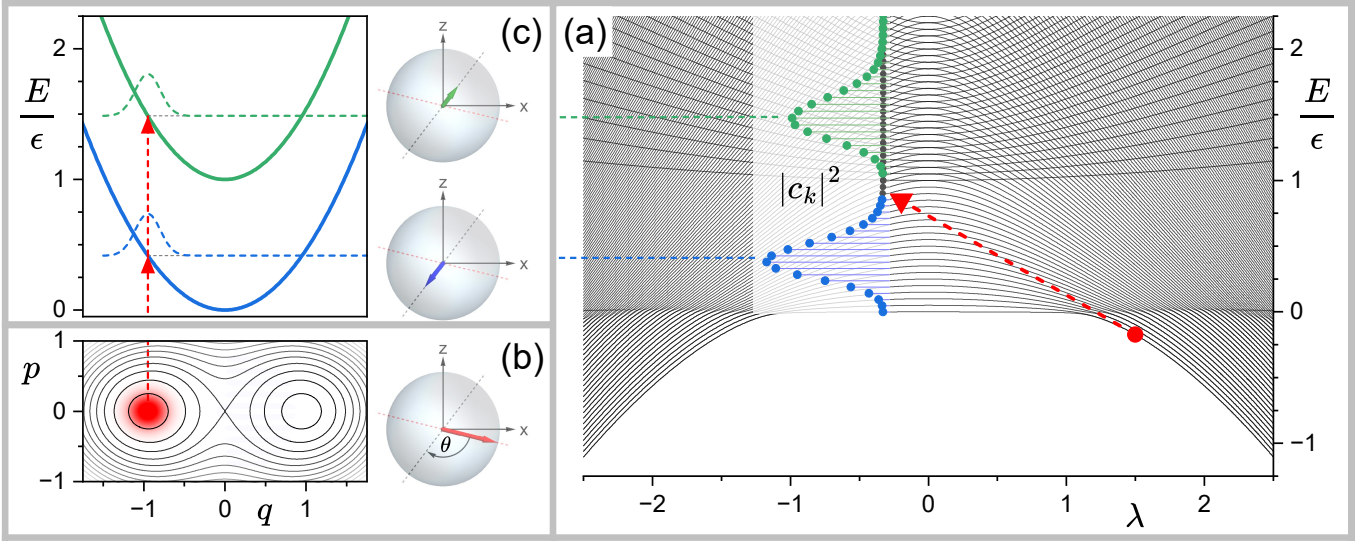


FIG. 2. (a) Spectrum (black lines) of Hamiltonian (1) and representation of the quench from Fig. 1 for $j = \frac{1}{2}$. The final energy distribution $|c_k|^2$ is split to blue and green parts corresponding to $m = -\frac{1}{2}$ and $+\frac{1}{2}$, respectively. (b) Oscillator Wigner function (red blob) on the energy contours of $\hat{H}_{\text{osc}}^{(-1/2)}$ (gray lines) and the spin orientation on the Bloch sphere at λ_{in} . (c) Cuts of the oscillator effective Hamiltonians $\hat{H}_{\text{osc}}^{(\pm 1/2)}$ (blue and green curves) and the spin orientation at λ_{fi} .

while the spin retains projection m to the moving direction $\mathbf{n}(t) = \mathbf{n}(\bar{q}(t), \bar{p}(t), \lambda)$, where $\bar{q}(t)$ and $\bar{p}(t)$ stand for the evolving oscillator coordinate-momentum averages.

The initial state $|\Psi_{\text{in}}\rangle \equiv |\Psi(0)\rangle$ has an approximately factorized form $|\Psi_{\text{in}}\rangle \approx |\psi_{\text{in}}\rangle \otimes |-j; \mathbf{n}_{\text{in}}\rangle$, where $|\psi_{\text{in}}\rangle$ is a displaced quasi-Gaussian state of the oscillator and $|-j; \mathbf{n}_{\text{in}}\rangle$ denotes the spin state with the minimal projection in the direction $\mathbf{n}_{\text{in}} \equiv \mathbf{n}(\bar{q}_{\text{in}}, \bar{p}_{\text{in}}, \lambda_{\text{in}})$ corresponding to the initial ground-state averages $\bar{q}_{\text{in}} = \langle \psi_{\text{in}} | \hat{q} | \psi_{\text{in}} \rangle$ and $\bar{p}_{\text{in}} = \langle \psi_{\text{in}} | \hat{p} | \psi_{\text{in}} \rangle$. This state cast in terms of the new spin direction $\mathbf{n}'_{\text{in}} = \mathbf{n}(\bar{q}_{\text{in}}, \bar{p}_{\text{in}}, \lambda_{\text{fi}})$, corresponding to the final strength λ_{fi} , reads as

$$|\Psi(0)\rangle \approx |\psi_{\text{in}}\rangle \otimes \left[\sum_{m=-j}^{+j} \underbrace{\langle m; \mathbf{n}'_{\text{in}} | -j; \mathbf{n}_{\text{in}} \rangle}_{\alpha^{(m)}} |m; \mathbf{n}'_{\text{in}}\rangle \right]. \quad (4)$$

The evolution of this state is then given by

$$|\Psi(t)\rangle \approx \sum_{m=-j}^{+j} \alpha^{(m)} \underbrace{[e^{-i\hat{H}_{\text{osc}}^{(m)}(\lambda_{\text{fi}})t} |\psi_{\text{in}}\rangle]}_{|\psi^{(m)}(t)\rangle} \otimes |m; \mathbf{n}^{(m)}(t)\rangle, \quad (5)$$

where the direction $\mathbf{n}^{(m)}(t) = \mathbf{n}(\bar{q}^{(m)}(t), \bar{p}^{(m)}(t), \lambda_{\text{fi}})$ is determined from moving coordinate and momentum ($\hat{x} \equiv \hat{q}, \hat{p}$) averages $\bar{x}^{(m)}(t) = \langle \psi^{(m)}(t) | \hat{x} | \psi^{(m)}(t) \rangle$. Since the effective oscillator Hamiltonians (3) for various projections m differ from each other, the initial wavepacket $|\psi_{\text{in}}\rangle$ splits into $n = 2j+1$ components $|\psi^{(m)}(t)\rangle$ moving in a different way, which can be seen in the phase-space representation $W_{\text{osc}}(q, p, t)$ of the oscillator state. The weights of these components are given by $|\alpha^{(m)}|^2$ and their partial coherence follows from the fact that the accompanying spin states $|m; \mathbf{n}^{(m)}(t)\rangle$ are not mutually orthogonal.

The above analysis is illustrated by an example in Fig. 2. Here, the system with $j = \frac{1}{2}$ is prepared in the initial state of the quench from Fig. 1. This state (a particular superposition of the quasidegenerate lowest energy parity doublet in the superradiant phase) is represented by the bullet in the energy spectrum $\{E_k(\lambda)\}$ in panel (a) and by the factorized oscillator-spin state in panel (b), where the oscillator Wigner function is located in one of two nearly degenerate minima of the classical $q \times p$ representation of $\hat{H}_{\text{osc}}^{(-1/2)}(\lambda_{\text{in}})$ while the spin points along the direction \mathbf{n}_{in} on the Bloch sphere. Parameter λ is then switched to a negative λ_{fi} in the normal phase. The arrow in panel (a) ends at the final energy average $\langle \Psi_{\text{in}} | \hat{H}_{\text{fi}} | \Psi_{\text{in}} \rangle$ and the histogram depicts the final energy distribution $|c_k|^2 = |\langle E_k(\lambda_{\text{fi}}) | \Psi_{\text{in}} \rangle|^2$. This distribution has two peaks centered at the mean energies of the initial state with respect to the new effective Hamiltonians $\hat{H}_{\text{osc}}^{(-1/2)}(\lambda_{\text{fi}})$ and $\hat{H}_{\text{osc}}^{(+1/2)}(\lambda_{\text{fi}})$, corresponding to the decomposition of the initial spin state to both projections along the new direction \mathbf{n}'_{in} , that forms angle θ with the original direction \mathbf{n}_{in} . The integral probability in both peaks is equal to the above-defined values $|\alpha^{(\pm 1/2)}|^2$. The $p = 0$ cuts of both $\hat{H}_{\text{osc}}^{(\pm 1/2)}(\lambda_{\text{fi}})$ and the new spin direction are shown in panel (c). This indicates the starting point of the after-quench evolution, when the initial state splits into the $m = \pm \frac{1}{2}$ parts, each of them composed of the oscillator wavepacket moving in the respective effective Hamiltonian $\hat{H}_{\text{osc}}^{(\pm 1/2)}(\lambda_{\text{fi}})$ and the spin keeping projection m to the evolving direction $\mathbf{n}^{(\pm 1/2)}(t)$ determined by the respective oscillator state.

In Fig. 3 we show the purity and the negativity

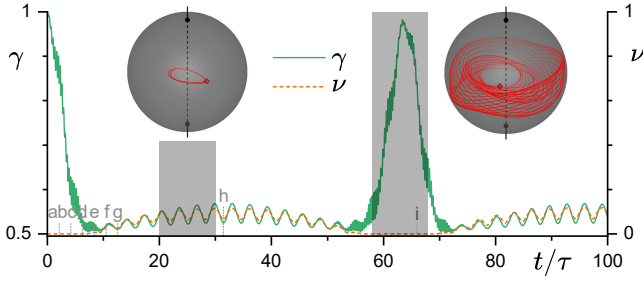


FIG. 3. Purity $\gamma(t)$ and negativity $\nu(t)$ after the quench from Fig. 1 for $j = \frac{1}{2}$. Inserted Bloch-sphere diagrams depict motions of the average spin $\langle \mathbf{J}(t) \rangle$ in two time intervals indicated by the gray zones.

of the oscillator state in a system with $j = \frac{1}{2}$ after the quench from Fig. 1. The purity $\gamma(t) = \text{tr } \hat{\rho}_{\text{osc}}^2(t)$ expresses the spin-oscillator entanglement [14], yielding values between $\gamma_{\min} = \frac{1}{2j+1}$ (for the maximally mixed oscillator state, i.e., maximally entangled total state $|\Psi(t)\rangle$) and $\gamma_{\max} = 1$ (for a pure oscillator state, i.e., fully factorized total state). The negativity $\nu(t) = \int [W_{\text{osc}}(q, p, t) - W_{\text{osc}}(q, p, t)] dq dp$ measures the negative volume of the oscillator Wigner function [50], quantifying the quantum coherence indicated by the ripples between individual wavepackets. We observe that the purity for $j = \frac{1}{2}$ oscillates at the level $\gamma - \gamma_{\min} \approx 0.1(\gamma_{\max} - \gamma_{\min})$ for most of time. For higher spins, the oscillations occur around higher values, e.g., $\gamma - \gamma_{\min} \approx 0.25(\gamma_{\max} - \gamma_{\min})$ for $j = 2$ [48]. On the other hand, the purity reaches the maximal value γ_{\max} within the time intervals when the negativity ν gets close to zero. Indeed, in these intervals both $m = \pm \frac{1}{2}$ wavepackets meet and overlap, so the spin-oscillator state becomes approximately factorized. As a consequence of the constructive addition of individual spin components in the overlap intervals, the average spin $\langle \mathbf{J}(t) \rangle \equiv \langle \Psi(t) | \hat{\mathbf{J}} | \Psi(t) \rangle$ grows from the interior of the Bloch sphere with radius j to its surface; see the second inset in Fig. 3. Simultaneously, the average spin exhibits very rapid precessional motions along the uniquely defined direction of $\mathbf{B}(\bar{q}, \bar{p}, \lambda)$.

The above method can be considered in connection with the preparation of specific cat-like states tailored to particular applications. The creation of such states starts by forming the initial state $|\Psi_{\text{in}}\rangle$, a superposition of the lowest Hamiltonian eigenstates at some λ_{in} , and continues by executing the prescribed quench $\lambda_{\text{in}} \rightarrow \lambda_{\text{fi}}$. When a suitable configuration of wavepackets in the oscillator phase space is reached, the protocol ends by turning off the spin-oscillator interaction, i.e., by the second quench $\lambda_{\text{fi}} \rightarrow 0$. Since then, all wavepackets will just periodically circulate in the intact potential of the harmonic oscillator. Figure 4 shows that parameters of the cat state can be fine tuned by changing the value of the final coupling strength of the first quench. The figure presents the weights of individual wavepackets and the

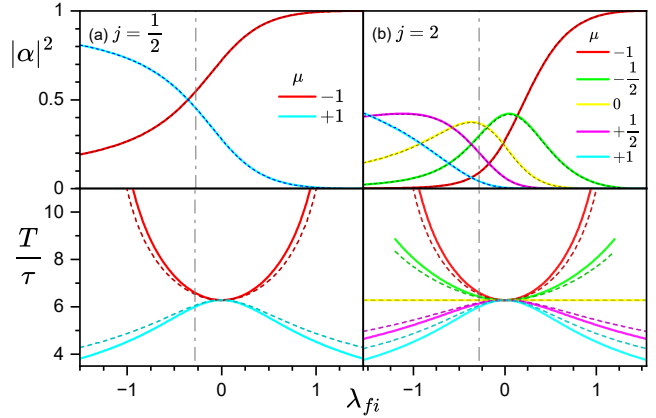


FIG. 4. Cat-state parameters for $\lambda_{\text{in}} = 1.5$ and variable λ_{fi} with (a) $j = \frac{1}{2}$ and (b) $j = 2$. Upper panels: Weights $|\alpha^{(m)}|^2$ of individual wavepackets from Eq. (4). Solid and dashed curves (practically coinciding) are calculated, respectively, from d -functions [48] and by summing $|c_k|^2$ in the corresponding peaks, cf. Fig. 2(a). Lower panels: Periods of classical orbits for $\mu = \frac{m}{j} = -1, \dots, +1$ and two values $\delta = 0.5$ (solid lines) and $\delta = 0$ (dashed lines). The vertical gray line indicates the quench used in the previous figures. We set $R = 50$.

periods of their motions as functions of λ_{fi} for $j = \frac{1}{2}$ and $j = 2$. We find that our cat-like states can be created in a large variety of proportions and dynamical relations, which is also demonstrated in the Supplemental Material and appended animations [48].

In conclusion, we have described a method of creating $(2j+1)$ -component cat-like states in a semiclassical oscillator coupled to spin of size j (to a set of $N = 2j$ qubits in an exchange-symmetric state). The protocol, which involves initialization of the spin-oscillator system in a superposition of the ground-state parity doublet in the superradiant phase and a subsequent quantum quench in the spin-oscillator coupling strength, allows for tuning of the cat-state parameters. The method is therefore capable of creating various motion configurations of a variable number of wave packets in different proportions. Despite their limited purity, these cat states in the phase-space representation show clear signatures of quantum coherence. They can be potentially applied in quantum information and sensing procedures involving qudits [51, 52].

Acknowledgments—Quantum dynamics was computed with the aid of the QuantumOptics.jl package [53]. We acknowledge financial support from the Czech Science Foundation under Project No. 25-16056S.

Data availability—The data that support the above findings can be obtained by openly available codes [54].

* pavel.stransky@matfyz.cuni.cz

† pavel.cejnar@matfyz.cuni.cz

[1] E. Schrödinger, Die gegenwärtige Situation in der Quantenmechanik (The Present Situation in Quantum Mechanics), *Naturwissenschaften*, **23**, 807 (1935).

[2] D.J. Wineland, Nobel Lecture: Superposition, entanglement, and raising Schrödinger's cat, *Rev. Mod. Phys.* **85**, 1103 (2013).

[3] K.G. Johnson, J.D. Wong-Campos, B. Neyenhuis, J. Mizrahi, and C. Monroe, Ultrafast creation of large Schrödinger cat states of an atom, *Nature Commun.* **8**, 697 (2017).

[4] F. Fröwis, P. Sekatski, W. Dür, N. Gisin, and N. Sangouard, Macroscopic quantum states: Measures, fragility, and implementations, *Rev. Mod. Phys.* **90**, 025004 (2018).

[5] A. Omran et al., Generation and manipulation of Schrödinger cat states in Rydberg atom arrays, *Science* **365**, 570 (2019).

[6] S.M. Girvin, Schrödinger cat states in circuit QED, in *Lecture Notes of the Les Houches Summer School, Session CVII—Current Trends in Atomic Physics 2016*, edited by A. Browaeys et al., p. 402 (Oxford University Press, Oxford, 2019).

[7] B. Hacker et al., Deterministic creation of entangled atom-light Schrödinger-cat states, *Nature Photon.* **13**, 110 (2019).

[8] Z. Wang et al., A flying Schrödinger's cat in multipartite entangled states., *Sci. Adv.* **8**, eabn1778 (2022).

[9] S. He, X. Xin, F.-Y. Zhang, and C. Li, Generation of a Schrödinger cat state in a hybrid ferromagnet-superconductor system, *Phys. Rev. A* **107** 023709 (2023).

[10] M. Bild et al., Schrödinger cat states of a 16-microgram mechanical oscillator, *Science* **380**, 274 (2023).

[11] A.Q. Batin, S. Ghosh, U. Roy, and D. Vitali, Engineering entangled Schrödinger cat states of separated cavity modes in cavity QED, *Phys. Rev. A* **110**, 043717 (2024).

[12] P. Gupta, A. Vaartjes, X. Yu, A. Morello, and B.C. Sanders, Robust macroscopic Schrödinger's cat on a nucleus, *Phys. Rev. Research* **6**, 013101 (2024).

[13] D. Hoshi et al., Entangling Schrödinger's cat states by bridging discrete- and continuous-variable encoding, *Nat Commun* **16**, 1309 (2025).

[14] M. A. Nielsen and I. L. Chuang, *Quantum Computation and Quantum Information* (Cambridge University Press, Cambridge, 2000).

[15] S. Haroche, Quantum information in cavity quantum electrodynamics: logical gates, entanglement engineering and 'Schrödinger-cat states', *Phil. Trans. R. Soc. A* **361**, 1339 (2003).

[16] M. Mirrahimi, Z. Leghtas, V.V. Albert, S.L. Touzard, R.J. Schoelkopf, L. Jiang, and M.H. Devoret, Dynamically protected cat-qubits: a new paradigm for universal quantum computation, *New J. Phys.* **16**, 045014 (2014).

[17] C. Flühmann, T.L. Nguyen, M. Marinelli, V. Negnevitsky, K. Mehta, and J.P. Home, Encoding a qubit in a trapped-ion mechanical oscillator, *Nature* **566**, 513 (2019).

[18] A. Grimm, N. E. Frattini, S. Puri, S. O. Mundhada, S. Touzard, M. Mirrahimi, S. M. Girvin, S. Shankar, and M.H. Devoret, Stabilization and operation of a Kerr-cat qubit, *Nature* **584**, 205 (2020).

[19] L. Gravina, F. Minganti, and V. Savona, Critical Schrödinger Cat Qubit, *PRX Quantum* **4**, 020337 (2023).

[20] X. Yu, B. Wilhelm, D. Holmes, et al., Schrödinger cat states of a nuclear spin qudit in silicon, *Nat. Phys.* **21**, 362 (2025).

[21] F. Toscano, D.A.R. Dalvit, L. Davidovich, and W.H. Zurek, Sub-Planck phase-space structures and Heisenberg-limited measurements, *Phys. Rev. A* **73**, 023803 (2006).

[22] H. Kwon, K.C. Tan, T. Volkoff, and H. Jeong, Nonclassicality as a quantifiable resource for quantum metrology, *Phys. Rev. Lett.* **122**, 040503 (2019).

[23] M. Tatsuta, Y. Matsuzaki, and A. Shimizu, Quantum metrology with generalized cat states, *Phys. Rev. A* **100**, 032318 (2019).

[24] B. Vlastakis et al., Characterizing entanglement of an artificial atom and a cavity cat state with Bell's inequality, *Nat Commun* **6**, 8970 (2015).

[25] B. Lajci, D.H. J. O'Dell, and J. Mumford, Topologically protected Bell-cat states in a simple spin model, *arXiv:2410.23532 [quant-ph]* (2024).

[26] J. Janszky, P. Domokos, and P. Adam, Coherent states on a circle and quantum interference, *Phys. Rev. A* **48**, 2213 (1993).

[27] N. Shukla, N. Akhtar, and B. C. Sanders, Quantum tetra-chotomous states: Superposition of four coherent states on a line in phase space, *Phys. Rev. A* **99**, 063813 (2019).

[28] L. A. Howard, T. J. Weinhold, F. Shahandeh, J. Combes, M. R. Vanner, A. G. White, and M. Ringbauer, Quantum hypercube states, *Phys. Rev. Lett.* **123**, 020402 (2019).

[29] T. Hailin, N. Akhtar, and G. Xianlong, Multicomponent cat states with sub-Planckian structures and their optomechanical analogues, *Phys. Rev. Applied* **24**, 024053 (2025).

[30] I.I. Rabi, On the Process of Space Quantization, *Phys. Rev.* **49**, 324 (1936); Space Quantization in a Gyrating Magnetic Field, *ibid.* **51**, 652 (1937).

[31] R.H. Dicke, Coherence in Spontaneous Radiation Processes, *Phys. Rev.* **93**, 99 (1954).

[32] E.T. Jaynes and F.W. Cummings, Comparison of quantum and semiclassical radiation theories with application to the beam maser, *Proc. IEEE* **51**, 89 (1963).

[33] P. Stránský, P. Cejnar, and R. Filip, Stabilization of product states and excited-state quantum phase transitions in a coupled qubit-field system, *Phys. Rev. A* **104**, 053722 (2021).

[34] P. Stránský, P. Cejnar, and R. Filip, Unitary collapse of Schrödinger's cat state, *Phys. Rev. A* **110**, L030202 (2024).

[35] P. Forn-Díaz, L. Lamata, E. Rico, J. Kono, and E. Solano, Ultrastrong coupling regimes of light-matter interaction, *Rev. Mod. Phys.* **91**, 025005 (2019).

[36] O. Di Stefano et al., Resolution of gauge ambiguities in ultrastrong-coupling cavity quantum electrodynamics, *Nature Phys.* **15**, 803 (2019).

[37] P. Campagne-Ibarcq et al., Quantum error correction of a qubit encoded in grid states of an oscillator, *Nature* **584**, 368 (2020).

[38] R. Stassi, M. Cirio, and F. Nori, Scalable quantum computer with superconducting circuits in the ultrastrong coupling regime, *npj Quantum Inf.* **6**, 67 (2020).

[39] J. Hastrup, K. Park, R. Filip, and U.L. Andersen, Unconditional Preparation of Squeezed Vacuum from Rabi Interactions, *Phys. Rev. Lett.* **126**, 153602 (2021).

[40] Y.-H. Chen, W. Qin, X. Wang, A. Miranowicz, and F. Nori, Shortcuts to Adiabaticity for the Quantum Rabi Model: Efficient Generation of Giant Entangled Cat States via Parametric Amplification, *Phys. Rev. Lett.*

126, 023602 (2021).

[41] A. Eickbusch et al., Fast universal control of an oscillator with weak dispersive coupling to a qubit, *Nature Phys.* **18**, 1464 (2022).

[42] V.V. Sivak et al., Model-Free Quantum Control with Reinforcement Learning, *Phys. Rev. X* **12**, 011059 (2022).

[43] C.S. Wang et al., Observation of Wave-Packet Branching through an Engineered Conical Intersection, *Phys. Rev. X* **13**, 011008 (2023).

[44] X. Pan et al., Protecting the Quantum Interference of Cat States by Phase-Space Compression, *Phys. Rev. X* **13**, 021004 (2023).

[45] P. Cejnar, P. Stránský, M. Macek, and M. Kloc, Excited-state quantum phase transitions, *J. Phys. A: Math. Theo.* **54**, 133001 (2021).

[46] M. Hillery, R.F. O'Connell, M.O. Scully, and E.P. Wigner, Distribution functions in physics: Fundamentals, *Phys. Rep.* **106**, 121 (1984).

[47] A. Polkovnikov, Phase space representation of quantum dynamics, *Ann. Phys.* **325**, 1790 (2010).

[48] See Supplemental Material one video file available as ancillary files in arXiv.

[49] M.A. Bastarrachea-Magnani, A. Relaño, S. Lerma-Hernández, B. López-del-Carpio, J. Chávez-Carlos, and J.G. Hirsch, Adiabatic invariants for the regular region of the Dicke model, *J. Phys. A: Math. Theor.* **50** 144002 (2017).

[50] A. Kenfack and K. Życzkowski, Negativity of the Wigner function as an indicator of non-classicality, *J. Opt. B: Quantum Semiclass. Opt.* **6**, 396 (2004).

[51] Y. Wang, Z. Hu, B.C. Sanders, and S. Kais, Qudits and High-Dimensional Quantum Computing, *Front. Phys.* **8**, 589504 (2020).

[52] Y.L. Len, T. Gefen, A. Retzker, and J. Kolodynski, Quantum metrology with imperfect measurements, *Nature Commun.* **13**, 6971 (2022).

[53] S. Krämer, D. Plankensteiner, L. Ostermann, and H. Ritsch, QuantumOptics.jl: A Julia framework for simulating open quantum systems, *Comp. Phys. Comm.* **227**, 109 (2018).

[54] <https://github.com/PavelStransky/MulticomponentCat>

Supplemental material: Creating multicomponent Schrödinger cat states in a coupled qubit-oscillator system

Pavel Stránský^{1,*} and Pavel Cejnar^{1,†}

¹*Institute of Particle and Nuclear Physics, Faculty of Mathematics and Physics, Charles University, V Holešovičkách 2, 18000 Prague, Czechia*

(Dated: December 30, 2025)

In this supplemental text, we provide additional details on the extended Rabi model, derivations of key formulas, and supplementary figures that support the findings presented in the main text of the paper in order to demonstrate the range of possible after-quench outcomes.

I. MODEL

We consider an extended version of the Rabi model (also called the generalized [1, 2], asymmetric [3] or anisotropic [4–10] Rabi or Dicke model) with the Hamiltonian parametrized as

$$\begin{aligned}\hat{H} &= \omega\hat{b}^\dagger\hat{b} + \omega R\hat{J}_z + 2\lambda\omega\sqrt{\frac{R}{8j}}\lambda\left[\left(\hat{b}^\dagger + \hat{b}\right)\hat{J}_x - i\delta\left(\hat{b}^\dagger - \hat{b}\right)\hat{J}_y\right] \\ &= \omega\hat{b}^\dagger\hat{b} + \omega R\hat{J}_z + \lambda\omega\sqrt{\frac{R}{8j}}\left[(1 + \delta)\left(\hat{b}^\dagger\hat{J}_- + \hat{b}\hat{J}_+\right) + (1 - \delta)\left(\hat{b}^\dagger\hat{J}_+ + \hat{b}\hat{J}_-\right)\right],\end{aligned}\quad (1)$$

where $\hat{\mathbf{J}} = (\hat{J}_x, \hat{J}_y, \hat{J}_z)$ is the quasispin operator of size j , \hat{b}, \hat{b}^\dagger are the field (oscillator) annihilation and creation operators, ω is the field frequency, $R \gg 1$ is the detuning between the quasispin and the oscillator, which also plays the role of the size parameter of the system [11], λ is the quasispin-field interaction strength, and δ interpolates between the ($\delta = 1$) Jaynes (Tavis)-Cummings regime, ($\delta = 0$) Rabi (Dicke) regime and ($\delta = -1$) anti-Jaynes (anti-Tavis)-Cummings regime.

The critical coupling—Quantum Phase Transition (QPT)—between the normal ($|\lambda| < 1$) and deformed ($|\lambda| > 1$) phases occurs at $\lambda_c = \pm 1$, independently of δ and j .

The whole Hamiltonian can be rescaled and shifted so that all its terms are dimensionless and the ground-state energy of the noninteracting configuration $E_0(\lambda = 0)$ vanishes:

$$\begin{aligned}\hat{h} &\equiv \frac{1}{2j\omega R}\left(\hat{H} + 2j\omega R\right) \\ &= \frac{1}{2jR}\hat{b}^\dagger\hat{b} + \frac{1}{2}\left(\hat{j}_z + 1\right) + \lambda\frac{1}{4j}\sqrt{\frac{1}{2jR}}\left[(1 + \delta)\left(\hat{b}^\dagger\hat{j}_- + \hat{b}\hat{j}_+\right) + (1 - \delta)\left(\hat{b}^\dagger\hat{j}_+ + \hat{b}\hat{j}_-\right)\right],\end{aligned}\quad (2)$$

where $\hat{j}_\bullet = \hat{J}_\bullet/j$. After introducing the coordinate and momentum by substituting $\hat{b} = \sqrt{jR}(\hat{q} + i\hat{p})$, the Hamiltonian becomes

$$\hat{h} = \frac{1}{2}\left(\hat{p}^2 + \hat{q}^2\right) - \frac{1}{jR} + \frac{1}{2} + \hat{\mathbf{b}} \cdot \hat{\mathbf{j}},\quad (3)$$

where the rescaled effective magnetic field, independent of the size parameter R , is

$$\hat{\mathbf{b}} \equiv \frac{\hat{\mathbf{B}}}{2R} = \left(\frac{\lambda}{\sqrt{2}}\hat{q}, -\frac{\lambda}{\sqrt{2}}\delta\hat{p}, \frac{1}{2}\right) = |\hat{\mathbf{b}}| \hat{\mathbf{n}}.\quad (4)$$

$\hat{\mathbf{B}}$ is the effective magnetic field defined in the main text and $\hat{\mathbf{n}}$ is the corresponding unit vector.

* pavel.stransky@matfyz.cuni.cz

† pavel.cejnar@matfyz.cuni.cz

In the classical limit $R \rightarrow \infty$, the classical Hamiltonian reads as

$$h_{\text{osc}}^{(\mu)}(p, q, \lambda) = \frac{1}{2}(p^2 + q^2) + \frac{1}{2} + \mu \sqrt{\frac{\lambda^2}{2}(q^2 + \delta^2 p^2) + \frac{1}{4}}, \quad (5)$$

where $\mu = m/j \in [-1, 1]$ and $m = -j, \dots, j$ is the quasispin projection in the inner frame whose orientation is given by vector \mathbf{B} (for more discussion see Ref. [11] and the main text).

II. QUANTUM QUENCH

The main conclusions of this work are based on the analysis of the dynamics after performing a quantum quench $\lambda_{\text{in}} \rightarrow \lambda_{\text{fi}}$ from a parity violating ground state of the deformed phase, $\lambda_{\text{in}} > 1$, into $\lambda_{\text{fi}} < \lambda_{\text{in}}$. The initial energy calculated semiclassically from the global minimum of the Hamiltonian (5) placed at

$$q_{\min}(\lambda) = \pm \sqrt{\frac{1}{2} \left(\lambda^2 - \frac{1}{\lambda^2} \right)}, \quad p_{\min}(\lambda) = 0 \quad (6)$$

is

$$e_{\min}(\lambda) \equiv h_{\text{osc}}^{(-1)}(p_{\min}, q_{\min}, \lambda) = -\frac{1}{4} \left(\lambda^2 + \frac{1}{\lambda^2} \right) + \frac{1}{2}. \quad (7)$$

Note that the global minimum is always located in $\mu = -1$ subspace [12] and both its energy and position are independent of δ and j .

The after-quench energy expectation value can be determined by the semiclassical Hellmann-Feynman formula

$$\begin{aligned} e_{\text{fi}}(\lambda_{\text{fi}}, \lambda_{\text{in}}) &= e_{\text{in}} + (\lambda_{\text{fi}} - \lambda_{\text{in}}) \frac{\partial h_{\text{osc}}^{(-1)}}{\partial \lambda}(p_{\min}, q_{\min}, \lambda_{\text{in}}) \\ &= \frac{1}{4} \left(\lambda_{\text{in}}^2 - \frac{3}{\lambda_{\text{in}}^2} \right) - \frac{1}{2} \lambda_{\text{fi}} \left(\lambda_{\text{in}} - \frac{1}{\lambda_{\text{in}}^3} \right) + \frac{1}{2}, \end{aligned} \quad (8)$$

where $e_{\text{in}} \equiv e_{\min}(\lambda_{\text{in}})$.

First, let us focus on the single-spin case $j = \frac{1}{2}$. The initial state is approximately the product state [13]

$$|\Psi(0)\rangle = |\psi_{\text{in}}\rangle |\downarrow_{\mathbf{b}_{\text{in}}}\rangle, \quad (9)$$

where $|\psi_{\text{in}}\rangle \equiv |q_{\min}\rangle$ is the coherent state of the oscillator at $q = q_{\min}, p = p_{\min} = 0$,

$$\mathbf{b}_{\text{in}} = \mathbf{b}(p_{\min}, q_{\min}, \lambda_{\text{in}}) = \left(\frac{\lambda_{\text{in}}}{\sqrt{2}} q_{\min}, 0, \frac{1}{2} \right) \quad (10)$$

is the effective magnetic field for state $|\psi_{\text{in}}\rangle$ and the spin points against the direction of this field; note that in the notation of the main text, $|\downarrow_{\mathbf{b}_{\text{in}}}\rangle \equiv |m = 1/2; \mathbf{n}_{\text{in}} = \mathbf{b}_{\text{in}}/|\mathbf{b}_{\text{in}}|\rangle$.

Immediately after the quench, the state is the same. Expanded in the basis of the Hamiltonian for λ_{fi} , it can be expressed as

$$|\Psi(0)\rangle = \alpha^{(-1)} |q_{\min}\rangle |\downarrow_{\mathbf{b}_{\text{fi}}}\rangle + \alpha^{(+1)} |q_{\min}\rangle |\uparrow_{\mathbf{b}_{\text{fi}}}\rangle, \quad (11)$$

with amplitudes

$$\alpha^{(-1)} = \cos \frac{\theta}{2} = \sqrt{\frac{1 - \cos \theta}{2}}, \quad (12a)$$

$$\alpha^{(+1)} = e^{i\phi} \sin \frac{\theta}{2} = e^{i\phi} \sqrt{\frac{1 + \cos \theta}{2}}, \quad (12b)$$

where θ, ϕ are the azimuthal and polar angles, respectively, of the effective magnetic field vector

$$\mathbf{b}_{\text{fi}} = \left(\frac{\lambda_{\text{fi}}}{\sqrt{2}} q_{\min}, 0, \frac{1}{2} \right) \quad (13)$$

with respect to the coordinate frame in which the initial magnetic field \mathbf{b}_{in} points along the z -axis. The azimuthal angle θ can be explicitly calculated as

$$\cos \theta = \frac{\mathbf{b}_{\text{in}} \cdot \mathbf{b}_{\text{fi}}}{|\mathbf{b}_{\text{in}}| |\mathbf{b}_{\text{fi}}|} = \frac{2\lambda_{\text{in}} \lambda_{\text{fi}} q_{\text{min}}^2 + 1}{\sqrt{(2\lambda_{\text{in}}^2 q_{\text{min}}^2 + 1)(2\lambda_{\text{fi}}^2 q_{\text{min}}^2 + 1)}} = \frac{1 + \lambda_{\text{fi}} \lambda_{\text{in}} \left(\lambda_{\text{in}}^2 - \frac{1}{\lambda_{\text{in}}^2} \right)}{\lambda_{\text{in}}^2 \sqrt{1 + \lambda_{\text{fi}}^2 \left(\lambda_{\text{in}}^2 - \frac{1}{\lambda_{\text{in}}^2} \right)}}, \quad (14)$$

and the coordinate systems can be chosen so that the polar angle is $\phi = 0$.

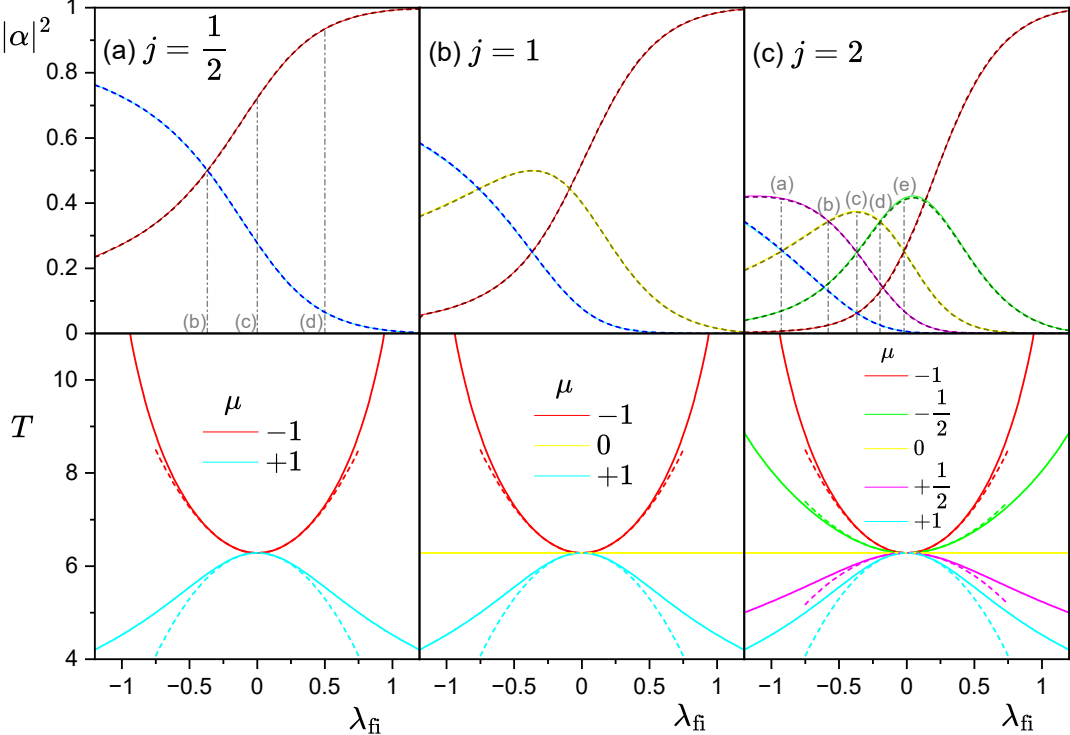


FIG. 1: *Top panels:* Squared amplitudes of the wavefunction contributions calculated from the Wigner d -functions (solid lines), see Eqs. (12) and (20), and from the strength function 26 (dashed lines), for three values of j . Gray vertical dash-dot lines indicate the quenches shown in Figs. 2 and 3. *Bottom panels:* Frequencies of the classical trajectories in all available subspaces $\mu = m/j$, $m = -j, \dots, j$. Solid and dashed lines, respectively, show exact results and the weak-interaction approximation (28). The initial coupling is $\lambda_{\text{in}} = 1.5$ and the size parameter is $R = 50$.

The expansion coefficients $\alpha^{(-1)}, \alpha^{(+1)}$ can also be determined entirely using semiclassical arguments. Final energy e_{fi} is composed of contributions from $\mu = \pm 1$ subspaces with weights $|\alpha^{(\pm 1)}|^2$. This leads to a set of equations

$$e_{\text{fi}} = \left| \alpha^{(-1)} \right|^2 h_{\text{osc}}^{(-1)}(q_{\text{min}}, 0, \lambda_{\text{fi}}) + \left| \alpha^{(+1)} \right|^2 h_{\text{osc}}^{(+1)}(q_{\text{min}}, 0, \lambda_{\text{fi}}), \quad (15)$$

$$\left| \alpha^{(-1)} \right|^2 + \left| \alpha^{(+1)} \right|^2 = 1, \quad (16)$$

whose solution gives exactly the same expressions as above, see Eq. (12) and Fig. 1(a).

One can ask which quench gives balanced contributions to both subspaces $\mu = \pm 1$ in the after-quench state, *i.e.*, which λ_{fi} results in $|\alpha^{(-1)}|^2 = |\alpha^{(+1)}|^2 = 1/2$. This happens when $\cos \theta = 0$, corresponding to the after-quench coupling

$$\lambda_{\text{fi}}^{(=)} \equiv \frac{\lambda_{\text{in}}}{1 - \lambda_{\text{in}}^4}. \quad (17)$$

The squared moduli of both $\alpha^{(-1)}$ and $\alpha^{(+1)}$ are shown by the solid lines in the first row of Fig. 1(a) for $\lambda_{\text{in}} = 1.5$. For this choice of the initial coupling, the moduli are equal when $\lambda_{\text{fi}}^{(=)} = -24/65 \approx -0.369$.

Another particular quench can be related to the presence of a stationary point in the classical Hamiltonian (5). The Hamiltonian in subspace $\mu = -1$ and in the deformed quantum phase $|\lambda_c| < |\lambda| < |\lambda_c/\delta|$ has a nondegenerate stationary point with index 1 (a saddle point). If a trajectory hits this point, *i.e.*, if $h_{\text{osc}}^{(-1)}(0, q_{\min}, \lambda_{\text{fi}}) = 0$, its period diverges. Since

$$h_{\text{osc}}^{(-1)}(0, q_{\min}, \lambda_{\text{fi}}) = \frac{1}{4} \left(\lambda_{\text{in}}^2 - \frac{1}{\lambda_{\text{in}}^2} \right) - \frac{1}{2} \sqrt{\lambda_{\text{fi}}^2 \left(\lambda_{\text{in}}^2 - \frac{1}{\lambda_{\text{in}}^2} \right) + 1} + \frac{1}{2}, \quad (18)$$

this *critical quench* is given by

$$\lambda_{\text{fi}}^{(c)} = \pm \sqrt{\frac{1}{4} \left(\lambda_{\text{in}}^2 - \frac{1}{\lambda_{\text{in}}^2} \right) + 1}. \quad (19)$$

For $\lambda_{\text{in}} = 3/2$, two possible critical quenches are $\lambda_{\text{fi}}^{(c)} = \pm \sqrt{209}/12 \approx \pm 1.205$. The evolution of the Wigner quasiprobability distribution after the quench with $\lambda_{\text{fi}} = -1.205$ is shown in the animation named *Dos gotas de Rabi* [14].

Last special quench discussed here is $\lambda_{\text{fi}} = -\lambda_{\text{in}}$, after which the part of the after-quench state in $\mu = -1$ subspace remains stationary in the initial minimum at $p = 0, q = q_{\min}$, since this point is also a minimum of the after-quench Hamiltonian due to the $h_{\text{osc}}^{(\mu)}(\lambda) = h_{\text{osc}}^{(\mu)}(-\lambda)$ symmetry. The animation of this quench is shown as *Rabiho rezonance dvou* [14].

Let us now extend the discussion to an arbitrary spin j . The expansion (11) in the λ_{fi} spin direction is given by the Wigner d -functions

$$\left| \Psi^{(j)}(0) \right\rangle = |q_{\min}\rangle \otimes \left[\sum_{m=-j}^j d_{m,-j}^{(j)}(\theta) |m\rangle \right], \quad (20)$$

where we use a shorthand notation $|m\rangle \equiv |m; \mathbf{n}'_{\text{in}} = \mathbf{b}_{\text{fi}} / |\mathbf{b}_{\text{fi}}|\rangle$. One can identify $\alpha^{(j,\mu)} \equiv d_{\mu j, -j}^{(j)}(\theta)$, where angle θ is given by Eq. (14). Examples for two values of $j > 1/2$ are:

• $j = 1$:

$$\left| \Psi^{(1)}(0) \right\rangle = |q_{\min}\rangle \left[\left(\cos \frac{\theta}{2} \right)^2 | -1 \rangle + \sqrt{2} \cos \frac{\theta}{2} \cos \frac{\theta}{2} | 0 \rangle + \left(\sin \frac{\theta}{2} \right)^2 | 1 \rangle \right] \quad (21)$$

• $j = 2$:

$$\begin{aligned} \left| \Psi^{(2)}(0) \right\rangle = & |q_{\min}\rangle \left[\left(\cos \frac{\theta}{2} \right)^4 | -2 \rangle + 2 \left(\cos \frac{\theta}{2} \right)^3 \sin \frac{\theta}{2} | -1 \rangle \right. \\ & + \sqrt{6} \left(\cos \frac{\theta}{2} \right)^2 \left(\sin \frac{\theta}{2} \right)^2 | 0 \rangle \\ & \left. 2 \cos \frac{\theta}{2} \left(\sin \frac{\theta}{2} \right)^3 | +1 \rangle + \left(\sin \frac{\theta}{2} \right)^4 | +2 \rangle \right] \end{aligned} \quad (22)$$

The corresponding squared moduli of the amplitudes $|\alpha^{(j,\mu)}|^2$ are shown in Fig. 1(b,c).

Note that

- Eq. (17) for equal contributions from the lowest and highest subspaces $\mu = \pm 1$ remains valid for any j ; this equation even holds for any pair of subspaces with $+\mu$ and $-\mu$.
- The critical quench (19) also remains unchanged for general j . On top of that, for higher values of j , there exists more subspaces with unstable stationary points at $p = q = 0$, see [11, 12], so there will be more critical quenches.
- The properties of the Wigner d -functions dictate that

$$\left| \alpha^{(j,\pm 1)} \right| = \left| \alpha^{(\frac{1}{2}, \pm 1)} \right|^{2j}. \quad (23)$$

The frequencies of classical trajectories in all available μ subspaces after the quench are given by the contour integral

$$T^{(\mu)} = \oint \frac{dq}{\dot{q}^{(\mu)}}, \quad (24)$$

where

$$\dot{q}^{(\mu)} \equiv \frac{\partial h_{\text{osc}}^{(\mu)}}{\partial p} = p \left[1 + \lambda^2 \delta^2 \mu \frac{1}{\sqrt{2\lambda^2(q^2 + \delta^2 p^2) + 1}} \right] \Big|_{h_{\text{osc}}^{(\mu)}(p, q, \lambda_{\text{fi}}) = h_{\text{osc}}^{(\mu)}(0, q_{\min}, \lambda_{\text{fi}})} \quad (25)$$

is the velocity of the oscillator coordinate in subspace μ . Since the energy e is measured in units $\epsilon \equiv 2jR\omega$, see Eq. (2), the period is expressed in units $\tau = \hbar/\epsilon$, where we fix $\hbar = 1$ in this study.

The frequencies are shown in the bottom row of Fig. 1(a) for $\lambda_i = 3/2$ and two values of δ . Note that the critical quench $\lambda_{\text{fi}}^{(c)} = \sqrt{209}/12 \approx 1.205$ with the divergent period is not shown in the Figure.

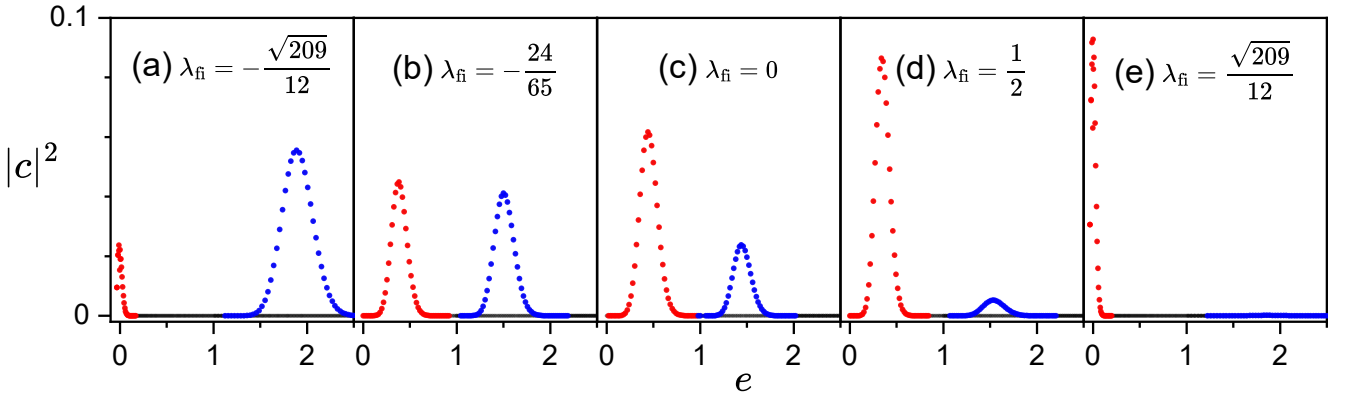


FIG. 2: Components of the strength function (26) for the Rabi model with $j = 1/2$, $\lambda_{\text{in}} = 1.5$, $R = 50$ and five different quenches. (a,e) Critical quenches (19) after which the stationary point in subspace $\mu = -1$ is hit (the frequency of the classical trajectory in this subspace is infinite). (b) Special quench (17) after which both the peaks of the strength function have the same magnitude. (c) Quench to the noninteracting configuration. (d) A generic quench corresponding to the animation named *Schnellbruder* [14].

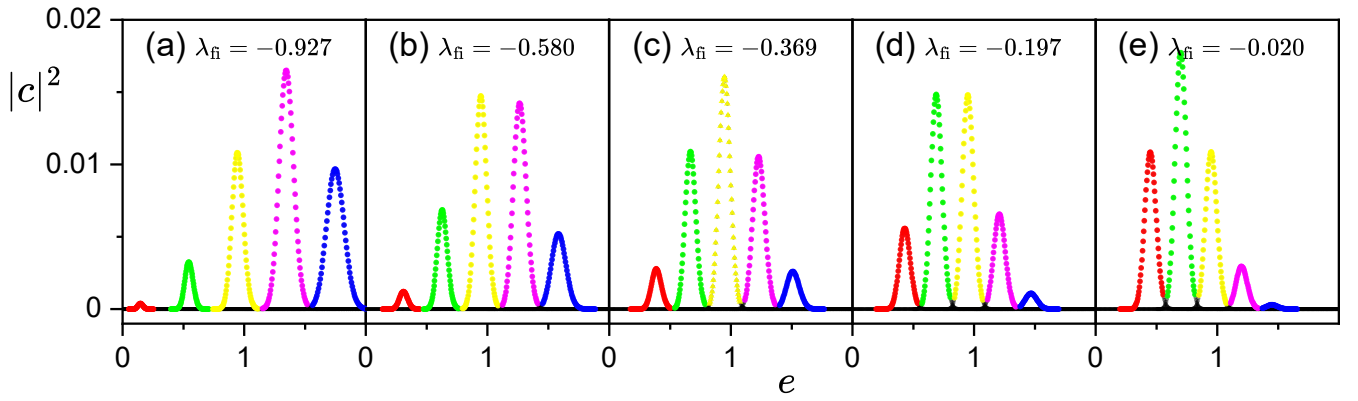


FIG. 3: Components of the strength function (26) for the Rabi model with $j = 2$, $\lambda_{\text{in}} = 1.5$ and $R = 50$ and five different quenches indicated by dash-dot lines in Fig. 1(c). Panel (c) corresponds to the animation of the Wigner quasiprobability distribution named *Five quantum brothers* [14].

Finally, let us focus on the structure of the after-quench strength function

$$S(e) = \sum_k \underbrace{\frac{|\langle e_k(\lambda_{\text{fi}}) | \Psi(0) \rangle|^2}{|c_k|^2}}_{\delta(e - e_k(\lambda_{\text{fi}}))} \quad (26)$$

where $|e_k(\lambda_{\text{fi}})\rangle$ are the eigenstates of the final quantum Hamiltonian $\hat{h}(\lambda_{\text{fi}})$ with corresponding rescaled energies $e_k(\lambda_{\text{fi}})$. In case $j = 1/2$ and $j = 2$, the strength function has 2 and 5 distinguishable peaks, see Figs. 2 and 3, respectively. The total strength of each peak, calculated as a partial sum of $|c_k|^2$ contributions displayed by different colors, corresponds to the squared amplitudes $|\alpha^{(\mu)}|^2$, as also shown in the top panel of Fig. 1.

III. SMALL COUPLING APPROXIMATION

For small values of the coupling constant $\lambda \ll 1$, the classical Hamiltonian (5) can be approximated by

$$\begin{aligned} h_{\text{osc}}^{(\mu)}(p, q) &= \frac{1}{2} (p^2 + q^2) + \frac{\mu}{2} \sqrt{2\lambda^2 (q^2 + \delta^2 p^2) + 1} \\ &\approx \frac{1}{2} [p^2 (1 + \mu\lambda^2 \delta^2) + q^2 (1 + \mu\lambda^2)], \end{aligned} \quad (27)$$

which is simply a harmonic oscillator with frequency

$$\begin{aligned} \omega^{(\mu)} &= \sqrt{(1 + \mu\lambda^2 \delta^2) (1 + \mu\lambda^2)} \\ &\approx 1 + \frac{\mu\lambda^2}{2} (1 + \delta^2). \end{aligned} \quad (28)$$

For $\lambda = \pm 2/5 = \pm 0.4$ and $\delta = 1/2$, the frequencies are

$$\omega^{(\mu)} \approx 1 + \frac{\mu}{10}, \quad (29)$$

which gives the ratios of frequencies in all available μ subspaces $9 : 11$, $9 : 10 : 11$, and $18 : 19 : 20 : 21 : 22$ for $j = 1/2, 1$, and 2 , respectively. The middle trajectory with $\mu = 0$ (not present when j is half-integer) has period $T_0 = 2\pi \approx 6.28$ (in units of τ). The trajectories with positive μ are faster, the ones with negative μ are slower.

In the main text of the paper, we select $\lambda_{\text{in}} = 1.5$, $\lambda_{\text{fi}} = -\sqrt{2}/5 \approx -0.283$, $\delta = 0.5$, which gives $\omega^{(\pm 1)} \approx 1 \pm 0.05$ and periods $T^{(-1)} \approx 6.60$ and $T^{(+1)} \approx 5.97$. Therefore, the two trajectories of subspaces $\mu = -1$ and $\mu = +1$ approximately meet at their initial positions at $t \approx 66$ (approximate revival) after 10 and 11 revolutions, respectively. This revival is captured in the Supplemental animations [15].

IV. APPROXIMATE FACTORIZATION AND FAST OSCILLATIONS

After quenches to $|\lambda_{\text{fi}}| < 1$, the state of the system approximately factorizes at a specific time τ ,

$$|\Psi(\tau)\rangle \approx |p(\tau), q(\tau)\rangle \otimes \sum_{\mu} \alpha^{(\mu)}(\tau) |\mu(\tau)\rangle, \quad (30)$$

where $|\mu(\tau)\rangle$ are eigenstates of the third component of the quasispin operator corresponding to quantum number $m = j\mu$ in the frame where the effective magnetic field $\mathbf{b}_{\text{fi}}(\tau)$ points along the z -axis. If we assume that $R \gg 1$, so that the spin motion is much faster and the oscillator can be adiabatically separated, then Hamiltonian (3) induces evolution

$$|\Psi(\tau + t)\rangle = |p(\tau), q(\tau)\rangle \otimes \sum_{\mu} \alpha^{(\mu)}(\tau) e^{i\mu|\mathbf{b}_{\text{fi}}(\tau)|t} |\mu(\tau)\rangle. \quad (31)$$

For a particular choice $j = 1/2$,

$$|\Psi(\tau + t)\rangle = |p(\tau), q(\tau)\rangle \otimes \left[\alpha^{(-1)}(\tau) e^{i|\mathbf{b}_{\text{fi}}(\tau)|t} |-1(\tau)\rangle + \alpha^{(+1)}(\tau) e^{-i|\mathbf{b}_{\text{fi}}(\tau)|t} |+1(\tau)\rangle \right], \quad (32)$$

so the “local survival probability”

$$P_{\tau}(t) \equiv |\langle \Psi(\tau) | \Psi(\tau + t) \rangle|^2 = 1 - 4 \left| \alpha^{(-1)}(\tau) \alpha^{(+1)}(\tau) \right|^2 \sin^2 (|\mathbf{b}_{\text{fi}}(\tau)| t) \quad (33)$$

oscillates with the Rabi frequency

$$\omega_{\tau} = |\mathbf{b}_{\text{fi}}(\tau)| \approx \frac{1}{2} \{ 1 + \lambda_{\text{fi}}^2 [q^2(\tau) + \delta^2 p^2(\tau)] \} \quad (34)$$

With the same frequency oscillates also the expectation values of the quasispin operator components [14, 15]

$$j_{k,\tau}(t) \equiv \langle \Psi(\tau + t) | \hat{j}_k | \Psi(\tau + t) \rangle. \quad (35)$$

V. PURITY AND WIGNER NEGATIVITY

The purity of the spin-oscillator system is defined as

$$\gamma(t) = \text{Tr} \hat{\rho}_{\text{osc}}^2(t), \quad (36)$$

where $\hat{\rho}_{\text{osc}}(t) = \text{Tr}_{\text{sp}} \hat{\rho}(t)$ is the reduced density matrix of the oscillator obtained by tracing out the spin degrees of freedom from the total density matrix $\hat{\rho}(t) = |\Psi(t)\rangle \langle \Psi(t)|$. It ranges from $\gamma = 1$ for a pure state to $\gamma = 1/(2j+1)$ for a maximally mixed state.

The Wigner negativity is given by

$$\nu(t) = \int |W_{\text{osc}}(q, p, t)| dq dp - 1, \quad (37)$$

where $W_{\text{osc}}(q, p, t)$ is the Wigner quasiprobability distribution of the oscillator at time t .

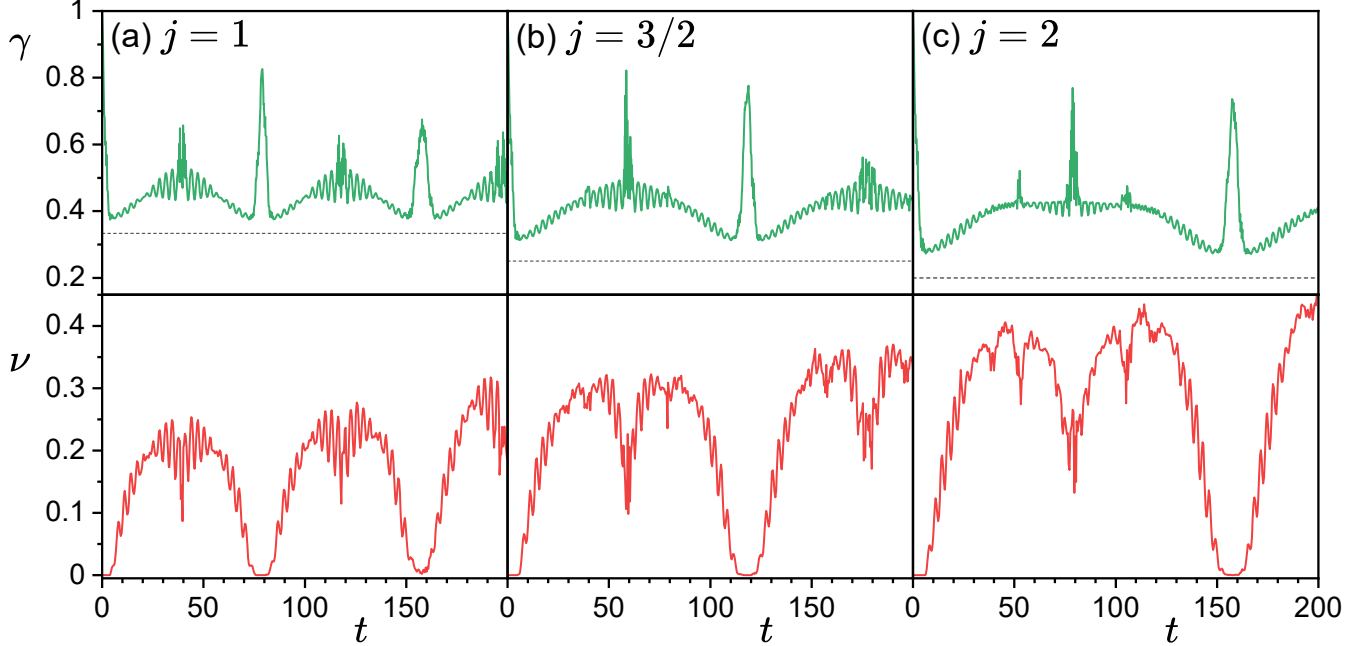


FIG. 4: Purity and negativity after quench $\lambda_{\text{in}} = 1.5 \rightarrow \lambda_{\text{fi}} = -0.369$ of the Rabi model with $R = 50$ and various spin sizes. Horizontal dashed lines in the purity panels indicate the minimum purity $1/(2j+1)$ for a maximally mixed state.

Both the purity and negativity are displayed in Fig. 4 for quench $\lambda_{\text{in}} = 1.5 \rightarrow \lambda_{\text{fi}} = -0.369$ and various values of j . We can see that the time evolution of the purity has a general trend: after an initial decay, it rises again and oscillates around a value that depends on j only weakly, hence increases relatively to the minimum purity $1/(2j+1)$ with increasing j , at least for small values of j . When the system is close to a revival, the purity reaches values close to 1, indicating that the spin and oscillator are nearly disentangled at these times. Due to gradual spreading of the wave packet, the revivals become less and less perfect for longer times.

On the other hand, the negativity vanishes at $t = 0$ and at the revivals, and is positive in the windows between the revivals. Its mean value in the inter-revival windows increases with j , which is caused by the increasing number $2j+1$ of the wavepackets (more components of the cat state) because each pair of subspace wavepackets creates one region of interference fringes with pronounced negativities and the number of wavepackets pairs grows quadratically with $2j+1$. The negativity also increases with time, which is caused by the wavepacket spreading and approaching state equilibration with necessary quantum fluctuations.

Next, let us discuss the scaling of the purity and negativity with the size parameter R , shown in Fig. 5. We observe that at the beginning of the evolution, the purity decays faster and the negativity starts rising sooner for larger R . However, between the initial decay and the first revival and in the subsequent inter-revival windows, both quantities seem to equilibrate around values that are almost independent of R , at least for not very high times, before the

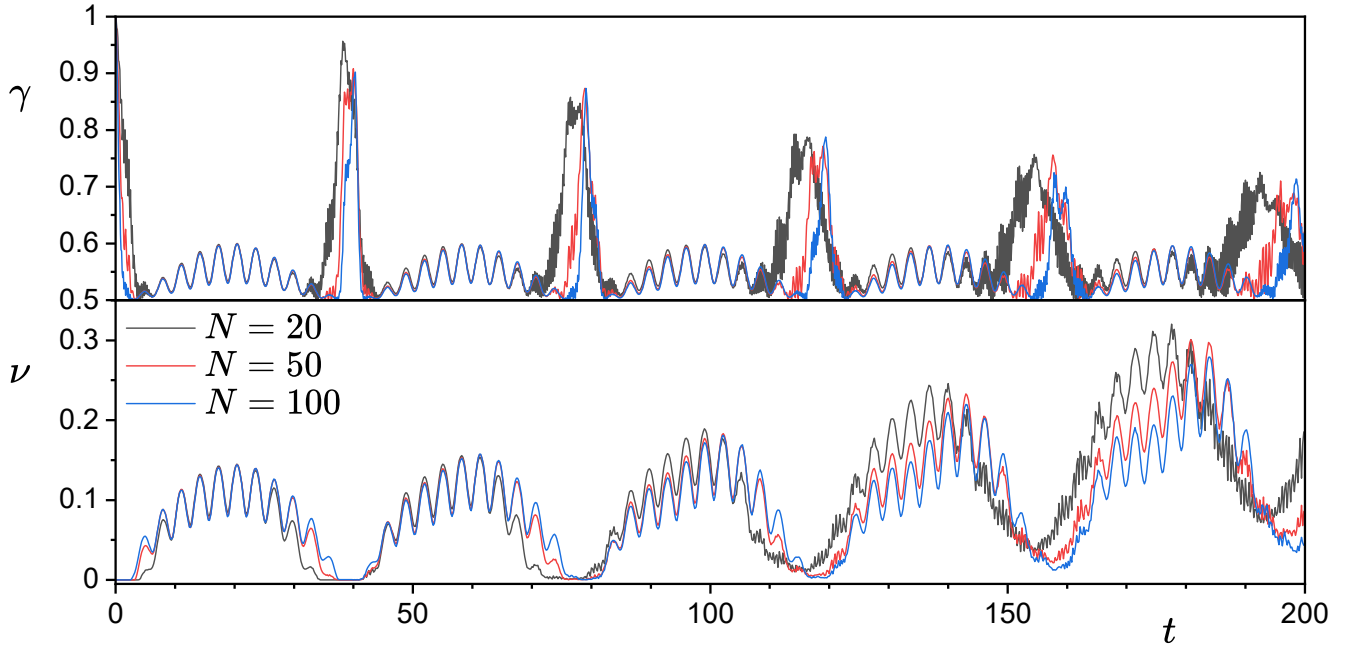


FIG. 5: Scaling of purity and negativity with size parameter R for quench $\lambda_{\text{in}} = 1.5 \rightarrow \lambda_{\text{fi}} = -0.369$ of the Rabi model with $j = 1/2$.

wavepacket spreading becomes significant. Note that the negativity is affected more strongly with the spreading due to increasing importance of the quantum fluctuations. The higher R , the narrower the wave packet and the later the appearance of the spreading effects.

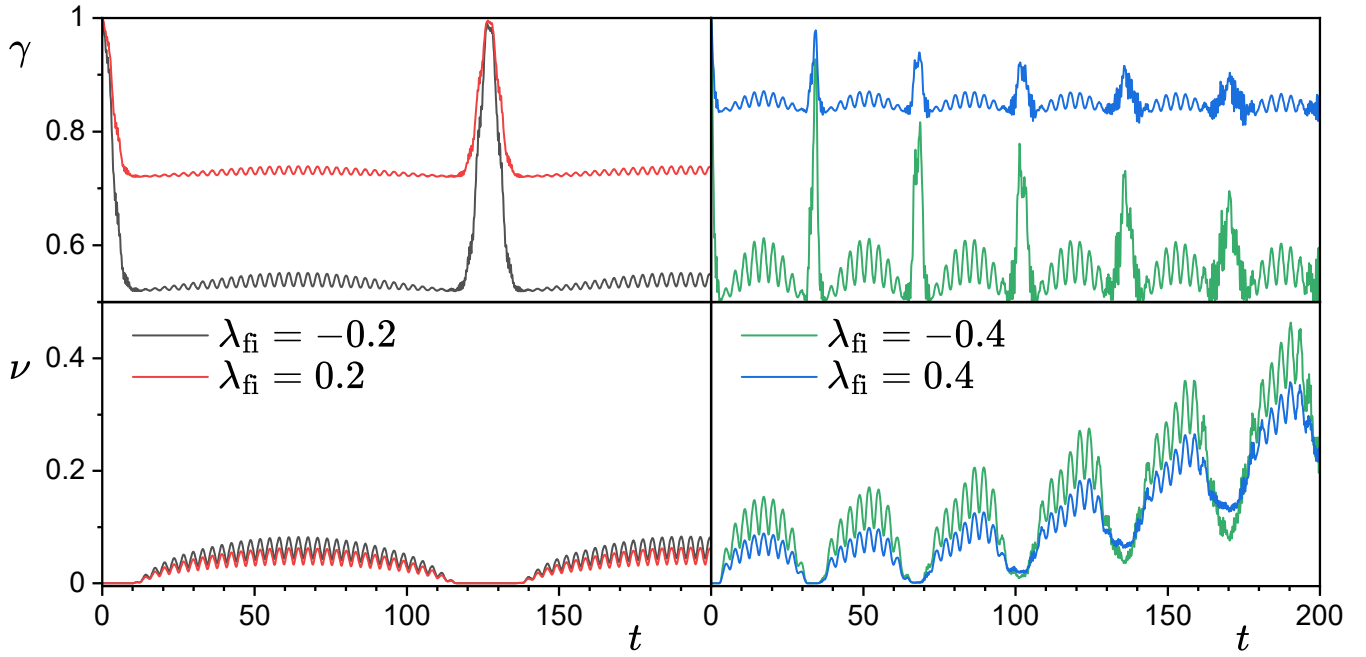


FIG. 6: Purity and negativity for various quenches $\lambda_{\text{in}} = 1.5 \rightarrow \lambda_{\text{fi}}$ of the Rabi model with $j = 1/2$ and $R = 50$.

Finally, we present the purity and negativity for various values of the after-quench coupling λ_{fi} in Fig. 6. It is observed that the revival times, indicated by $\gamma \approx 1$ and $\nu \approx 0$, and frequencies of the inter-revival oscillations are

independent of the sign of λ_{fi} —a fact related to the symmetry $h_{\text{osc}}^{(\mu)}(\lambda) = h_{\text{osc}}^{(\mu)}(-\lambda)$ of the semiclassical Hamiltonian (5). However, the weights of the individual subspace contributions in the after-quench state depend on λ_{fi} , recall Eq. (12), Fig. 1 and the strength function in Fig. 2. This leads to higher average the purity and negativity inside the inter-revival time intervals for quenches with more balanced contributions from both subspaces, *i.e.*, quenches with λ_{fi} close to $\lambda_{\text{fi}}^{(=)}$, because it is the interference between the subspace wavepackets that makes the state nonclassical with higher values of the Wigner negativity. The figure also shows that the quenches to very small values of $|\lambda_{\text{fi}}|$ lead to very long revival times, in accordance with the small-coupling approximation discussed above, and at the same time to slower wavepacket spreading and equilibration.

VI. DESCRIPTION OF SUPPLEMENTAL ANIMATIONS

There are two independent lists of animations demonstrating the dynamics of the Wigner function and mean values of some operators after the quench. All the animations share the following parameters: $\lambda_{\text{in}} = 1.5$, $\delta = 1/2$.

First, the animations corresponding to the quenches presented in the main text of the paper are shown in the Supplemental material [15]. These animations have $\lambda_{\text{fi}} = -0.283$ and size $R = 20$ and differ by the value of j : $j = 1/2, 1, 2$.

Second, additional animations are presented in a dedicated YouTube channel [14]. These animations have been made more attractive and funny by adding AI generated music with AI written lyrics in various languages. They are:

- **Schnellbruder**: $j = 1/2$, $\lambda_{\text{fi}} = 0.5$.
- **Dos gotas de Rabi**: $j = 1/2$, $\lambda_{\text{fi}} = \lambda_{\text{fi}}^{(c)} \approx 1.205$ (the wavepacket in $\mu = -1$ subspace eventually hits the stationary point at $p = q = 0$).
- **Rabiho rezonance dvou**: $j = 1/2$, $\lambda_{\text{fi}} = -\lambda_{\text{in}} = -1.5$ (the wavepacket in $\mu = -1$ subspace remains sitting in the initial minimum at $p = 0, q = q_{\text{min}}$).
- **Three quantum brothers**: $j = 1$, $\lambda_{\text{fi}} = \lambda_{\text{fi}}^{(=)} \approx 0.369$.
- **Five quantum brothers**: $j = 2$, $\lambda_{\text{fi}} = \lambda_{\text{fi}}^{(=)} \approx 0.369$.

The layout of all the animations (both from the Supplemental material and YouTube) is the same and contains the following panels:

- The main panel shows the Wigner quasiprobability distribution of the oscillator with its q and q marginals (squared moduli of the wave functions in q and p representations) displayed on the top and right sides of the panel, respectively. Time t is given in the panel caption. The bullets indicate the positions of the classical oscillator (solution of equations of motion given by the Hamiltonian (5)) in all available μ subspaces. The lines preceding the bullets show the last 10 time units (expressed in units of τ) of the classical trajectories. The classical evolution is projected onto the Bloch sphere (right-bottom panel) using the classical version of Eq. (4).
- The panels labelled J_x, J_y, J_z show the quantum expectation values of the quasispin operator components,

$$J_k(t) = \langle \Psi(t) | \hat{J}_k | \Psi(t) \rangle, \quad k = x, y, z. \quad (38)$$

The vector whose components are given by scaled values $J_k(t)/j$ is also displayed on the Bloch sphere (right-bottom panel, gray diamond and gray line).

- The panels labelled q, p show the expectation values of the quantum oscillator coordinates and momenta,

$$q(t) = \langle \Psi(t) | \hat{q} | \Psi(t) \rangle, \quad p(t) = \langle \Psi(t) | \hat{p} | \Psi(t) \rangle. \quad (39)$$

The corresponding normalized vector $\hat{\mathbf{n}}$ determined by Eq. (4) is shown on the Bloch sphere as the red square and its history as the red line.

- The panel labelled P shows the survival probability

$$P(t) = \left| \langle \Psi(0) | e^{-i\hat{h}(\lambda_{\text{fi}})t} | \Psi(0) \rangle \right|^2. \quad (40)$$

[1] F. T. Hioe, *Physical Review A* **8**, 1440 (1973).

[2] M. Tomka, O. El Araby, M. Pletyukhov, and V. Gritsev, *Physical Review A* **90**, 063839 (2014).

[3] L.-T. Shen, Z.-B. Yang, M. Lu, R.-X. Chen, and H.-Z. Wu, *Applied Physics B* **117**, 195 (2014).

[4] Q.-T. Xie, S. Cui, J.-P. Cao, L. Amico, and H. Fan, *Physical Review X* **4**, 021046 (2014).

[5] Y. Zhang and M. I. Dykman, *Physical Review A* **95**, 053841 (2017).

[6] M. Liu, S. Chesi, Z.-J. Ying, X. Chen, H.-G. Luo, and H.-Q. Lin, *Physical Review Letters* **119**, 220601 (2017).

[7] L.-T. Shen, Z.-B. Yang, H.-Z. Wu, and S.-B. Zheng, *Physical Review A* **95**, 013819 (2017).

[8] W. Buijsman, V. Gritsev, and R. Sprik, *Physical Review Letters* **118**, 080601 (2017).

[9] P. Das, D. S. Bhakuni, L. F. Santos, and A. Sharma, *Physical Review A* **108**, 063716 (2023).

[10] X. Zhu, J.-H. Lü, W. Ning, L.-T. Shen, F. Wu, and Z.-B. Yang, *Physical Review A* **109**, 052621 (2024).

[11] P. Stránský, P. Cejnar, and R. Filip, *Physical Review A* **104**, 053722 (2021).

[12] M. A. Bastarrachea-Magnani, A. Relaño, S. Lerma-Hernández, B. López-del Carpio, J. Chávez-Carlos, and J. G. Hirsch, *Journal of Physics A: Mathematical and Theoretical* **50**, 144002 (2017).

[13] R. Puebla, *Physical Review B* **102**, 220302 (2020).

[14] Animations of the Wigner quasiprobability distribution are available on the public YouTube channel <https://www.youtube.com/playlist?list=PLbYyGUIyYU9oRzAqMXd47A2M8ENA4Aumw>. They are accompanied by AI generated songs (text by ChatGPT, music by suno.com).

[15] Animations of the Wigner quasiprobability distribution provided directly in the Supplemental Material.